

A SEARCH FOR VERY EXTENDED IONIZED GAS IN NEARBY STARBURST AND ACTIVE GALAXIES

S. VEILLEUX

Department of Astronomy, University of Maryland, College Park, MD 20742;
veilleux@astro.umd.edu

P. L. SHOPBELL

Department of Astronomy, California Institute of Technology, Pasadena, CA, 91125

D. S. RUPKE³

Department of Astronomy, University of Maryland, College Park, MD 20742

J. BLAND-HAWTHORN⁵

Anglo-Australian Observatory, P.O. Box 296, Epping, NSW 2121, Australia

G. CECIL³

Department of Physics and Astronomy, CB #3255, University of North Carolina, Chapel Hill, NC 27599-3255

Draft version October 29, 2018

ABSTRACT

We report the results from a pilot study of 10 nearby starburst and active galaxies conducted with the Taurus Tunable Filter (TTF) on the Anglo-Australian and William Herschel Telescopes. The main purpose of this imaging survey is to search for warm emission-line gas on the outskirts (galactocentric distances $R \gtrsim 10$ kpc) of galaxies to provide direct constraints on the size and geometry of the “zone of influence” of these galaxies on their environment. Gaseous complexes or filaments larger than ~ 20 kpc are discovered or confirmed in six of the galaxies in the sample (NGC 1068, NGC 1482, NGC 4388, NGC 6240, NGC 7213, and MR 2251–178). Slightly smaller structures are seen for the first time in the ionization cones and galactic winds of NGC 1365, NGC 1705, Circinus galaxy, and ESO484-G036. The TTF data are combined with new optical long-slit spectra as well as published and archived radio and X-ray maps to constrain the origin and source of ionization of these filaments. A broad range of phenomena is observed, including large-scale ionization cones and galactic winds, tidal interaction, and ram-pressure stripping by an intracluster medium. The source of ionization in this gas ranges from shock ionization to photoionization by the central AGN or in-situ hot young stars. The sample is too small to draw statistically meaningful conclusions about the extent and properties of the warm ionized medium on large scale and its relevance to galaxy formation and evolution. The next generation of tunable filters on large telescopes promises to improve the sensitivity to faint emission-line fluxes at least tenfold and allow systematic surveys of a large sample of emission-line galaxies.

Subject headings: galaxies: active — galaxies: individual (NGC 1068, NGC 1365, NGC 1482, NGC 1705, NGC 4388, NGC 6240, NGC 7213, Circinus Galaxy, ESO484-G036, , and MR 2251–178) — galaxies: ISM — galaxies: kinematics and dynamics — galaxies: starburst — intergalactic medium

1. INTRODUCTION

The need for a comprehensive survey of the warm ionized medium in the local universe can hardly be overstated. This gas phase may contribute significantly to the local baryon budget (e.g., Fukugita, Hogan, & Peebles 1998), but very little is known about its distribution. While an important fraction of this material is almost certainly in the form of intergalactic clouds not related to any individual galaxy, some may inhabit the dark matter halos of galaxies (e.g., Rauch 1998).

This gas phase is a key witness to galaxy formation and evolution. In a hierarchical CDM universe (e.g., Jenkins et al. 1998) most of the activity associated with galaxy formation

takes place at $z \gtrsim 1$, except perhaps in the outer reaches of galaxies where “primordial” gas may still be accreting today. Some of this material will necessarily be ionized by the metagalactic ionizing radiation, and possibly also by local sources of ionizing radiation such as active galactic nuclei (AGN) and starbursting stellar populations. In this picture, the warm ionized gas on the outskirts of galaxies represents left-over debris associated with galaxy formation (e.g., Bland-Hawthorn 1999; Blitz et al. 1999).

The warm ionized gas is also an excellent probe of the feedback processes taking place in galaxies. Ionizing radiation and mechanical energy from star-forming regions and quasars may severely limit the amount of star formation and affect galaxy

¹ Current Address: 320-47 Downs Lab., Caltech, Pasadena, CA 91125 and Observatories of the Carnegie Institution of Washington, 813 Santa Barbara Street, Pasadena, CA 91101; veilleux@ulirg.caltech.edu

² Cottrell Scholar of the Research Corporation

³ Visiting Astronomer, Anglo-Australian Observatory, P.O. Box 296, Epping, NSW 1710, Australia

⁴ Visiting Astronomer, Mount Stromlo and Siding Springs Observatory, operated by the Research School of Astronomy and Astrophysics, Cotter Road, Weston Creek, Canberra, ACT72611, Australia

⁵ Visiting Astronomer, William Herschel Telescope, Isaac Newton Group of Telescopes, Observatorio Roque de Los Muchachos, Santa Cruz de la Palma, Canary Islands E-38700, Spain

evolution. The emerging radiation field defines regions where gas is warm and ionized (e.g., “proximity effect” in quasars and Lyman-break galaxies and “ionization cones” in nearby active and starburst galaxies; e.g., Bajtlik, Duncan, & Ostriker 1988; Steidel, Pettini, & Adelberger 2001; Wilson & Tsvetanov 1994). Galactic winds may blow out through the gaseous halos of galaxies and into the IGM, enriching and heating the intergalactic environment in the process. These winds may be responsible for the well-known mass-metallicity relation in galaxies (e.g., Larson & Dinerstein 1975; Vader 1986; Franx & Illingworth 1990). The discovery of $\text{H}\alpha$ filaments and diffuse soft X-ray emission out to 11.6 kpc from the prototypical starburst/superwind galaxy M82 (Devine & Bally 1999; Lehnert, Heckman, & Weaver 1999; Stevens, Read, & Bravo-Guerrero 2003) emphasizes the need for surveying large areas around superwind galaxies to constrain the size, energetics, and impact of these superwinds. The large “cavities” in the X-ray surface brightness of several cooling flow clusters with radio-loud cD galaxies (e.g., Böhringer et al. 1993; Fabian et al. 2000; McNamara et al. 2000; Fabian 2001; Quilis, Bower, & Balogh 2001; Heinz et al. 2002) point to equally large zones of influence for AGN-driven outflows. Galactic winds in the early universe are likely to have had an even stronger influence on the environment (e.g., Alderberger et al. 2003; Shapley et al. 2003).

The present paper describes the results from a pilot survey of 10 nearby starburst and active galaxies with the Taurus Tunable Filter (TTF) on the Anglo-Australian and William Herschel Telescopes. The main goals of this survey are to search for warm ($T \approx 10^4$ K) line-emitting gas on the outskirts of these galaxies, and study the properties of this gas to constrain its origin and overall importance. The names, redshifts, and nuclear types of the galaxies in the sample are listed in Table 1 along with a summary of the findings from the TTF survey. These galaxies were selected based on the fact that they all present ionization cones and/or galactic winds on \sim kpc scale. This method of selection and the small number of galaxies in the sample imply that this sample is probably not representative of the local population of starburst/active galaxies, and therefore should not be used for statistical purposes. Nevertheless, the results from this pilot survey should provide important clues on the range of phenomena taking place in the general local galaxy population.

This paper is organized as follows. In §2, we discuss the methods of observations. The results are described individually for each object in §3. In §4, we summarize the results and discuss future avenues of research. The present discussion complements recent Fabry-Perot searches for warm ionized gas on the outskirts of “normal” galaxies including our own Galaxy (e.g., Bland-Hawthorn et al. 1998; Putman et al. 2003) and several dwarf, spiral, and elliptical galaxies (e.g., Bland-Hawthorn, Freeman, & Quinn 1997a; Meurer et al. 1999; Ferguson, van der Hulst, & van Gorkom 2001; Miller & Veilleux 2003a, 2003b), as well as in isolated extragalactic H I clouds (e.g., Weymann et al. 2001) and a few active galaxies with collimated jet outflows (e.g., Cecil et al. 2000; Tadhunter et al. 2000). The results in the present paper supersede those from Veilleux (2002). The results for two of the galaxies in the sample have already been presented elsewhere (NGC 1482: Veilleux & Rupke 2002; MR 2251–178: Shopbell, Veilleux, & Bland-Hawthorn 1999), but are discussed again in the present paper for the sake of completeness and to add to the discussion (e.g., a new unpublished X-ray map of NGC 1482 are presented

here along with a deeper reprocessed $\text{H}\alpha$ + [N II] $\lambda 6583$ image of this object).

2. OBSERVATIONS

The TTF on the 3.9-meter Anglo-Australian Telescope (AAT) was used for all but one of the observations reported in the present paper. The TTF on the 4.2-meter William Herschel Telescope (WHT) was used for NGC 1068. The TTF is described in detail in Bland-Hawthorn & Jones (1998) and Bland-Hawthorn & Kedziora-Chudczer (2003). The data acquisition and reduction techniques used to reach low flux levels with the TTF have already been discussed in several papers (e.g., Shopbell et al. 1999; Glazebrook & Bland-Hawthorn 2001; Veilleux & Rupke 2002; Jones, Shopbell, & Bland-Hawthorn 2002; Miller & Veilleux 2003a). The TTF is uniquely suited to carry out deep searches for emission-line gas on the outskirts of galaxies, combining wide field of view ($\sim 10'$) with outstanding narrow-band imaging capabilities over a broad range in wavelength (3500 Å – 1.0 μm) and bandpass (10 – 100 Å). A summary of the TTF observations is given in Tables 2 and 3. Nearly all of the AAT observations were carried out in the “charge shuffling/frequency switching” mode, where the charges are moved up and down within the detector at the same time as switching between two discrete frequencies with the tunable filter. The charges were generally moved every minute and the chip was read after typically spending 32 minutes of integration time (16 minutes on-band and 16 minutes off-band). As a result, the continuum and emission-line images are produced nearly simultaneously, therefore averaging out temporal variations associated with atmospheric lines and transparency, seeing, instrument and detector instabilities. Most of the AAT images were obtained in a straddle mode, where the off-band image is made up of a pair of images that “straddle” the on-band image in wavelength (e.g., $\lambda_1 = 6500$ Å and $\lambda_2 = 6625$ Å for rest-frame $\text{H}\alpha$); this greatly improves the accuracy of the continuum removal since it corrects for slopes in the continuum and underlying absorption features. The charge shuffling and frequency switching capabilities were not available at the WHT. The flux levels reached by the TTF observations are listed in the last column of Table 3.

Long-slit optical spectra were also obtained for some of the objects to clarify the origin and source of ionization of the warm ionized material. Tables 2 and 4 summarize the details of these observations. These spectra were reduced using standard IRAF routines. When available, complementary X-ray and radio maps were used to track the hot (X-rays), relativistic (20-cm) and neutral (HI) gas phases in the sample galaxies and allow us to draw a more complete picture of these objects.

3. RESULTS

3.1. NGC 1068

NGC 1068 is arguably the best studied active galaxy in the local universe. It is a Sb galaxy which is nearly face-on ($i \approx 30$; de Vaucouleurs et al. 1991) and shows evidence for a ~ 3 -kpc bar (e.g., Scoville et al. 1988; Thronson et al. 1989; Helfer & Blitz 1995). Signs of the AGN in the core of this galaxy are evident at nearly all wavelengths. It was one of the six objects originally studied by Seyfert (1943) with bright optical “emission lines similar to those in planetary nebulae.” Four decades later, spectropolarimetry of NGC 1068 revealed the presence of broad ($\text{FWHM} \approx 4,500 \text{ km s}^{-1}$) recombination lines in scattered light, suggesting for the first time that the \lesssim

pc-scale broad line region in this object is obscured by an optically thick torus (e.g., Miller & Antonucci 1983; Antonucci & Miller 1985; Miller, Goodrich, & Mathews 1991). Indirect evidence for a inner disk structure in NGC 1068 comes from the presence of bright cones of photoionized gas detected at optical wavelengths (e.g., Baldwin, Wilson, & Whittle 1987; Pogge 1988a; Macchetto et al. 1994; Kraemer, Ruiz, & Crenshaw 1998) and also in X-rays (e.g., Young, Wilson, & Shopbell 2001; Kinkhabwala et al. 2002). The ionization cones are roughly aligned with the inner radio jet and large-scale radio structure (e.g., Wilson & Ulvestad 1987; Gallimore et al. 1996). Most of the inner line-emitting clouds originally discovered by Walker (1968) are taking part in a large-scale outflow event (e.g., Cecil, Bland, & Tully 1990; Arribas, Mediavilla, & Garcia-Lorenzo 1996; Crenshaw & Kraemer 2000). Some of the line-emitting material near the nucleus is outflowing at velocities of up to $\sim 3200 \text{ km s}^{-1}$ (Cecil et al. 2002b); this material appears to be accelerated radiatively by the AGN (Dopita et al. 2002). UV line ratios are inconsistent with shock excitation (Groves et al., in prep.).

The anisotropic radiation field from the AGN in NGC 1068 is already known to affect the inner $\sim 10 \text{ kpc}$ diameter disk of the host galaxy (Bland-Hawthorn, Sokolowski, & Cecil 1991; Sokolowski, Bland-Hawthorn, & Cecil 1991). Our new data on NGC 1068 now show that the ionization cone extends even further. Figure 1 presents deep $\text{H}\alpha$ and $[\text{O III}] \lambda 5007$ images obtained with the TTF. A complex of knots and filaments are detected out to $R \approx 11 \text{ kpc}$ along $\text{P.A.} \approx 15^\circ - 70^\circ$. Another fainter complex is seen out to $\sim 10 \text{ kpc}$ in the opposite direction at $\text{P.A.} \approx 200^\circ - 260^\circ$. There is a deficit of filaments in all other directions.

Figure 2 compares the locations of the filaments with an unpublished H I 21-cm map graciously provided to us by E. Brinks (2003; private communication). Some of the optical filaments (especially those to the south-west) lie slightly beyond the sharp H I “edge” of NGC 1068. As in the case of NGC 253 (Bland-Hawthorn et al. 1997a), the filaments are too bright to be photoionized solely by the metagalactic ionizing radiation – another source of ionization is needed. The surprisingly bright $\text{H}\alpha$ emission beyond the H I edge of NGC 253 is probably due to photoionization by hot young stars in the inner disk (Bland-Hawthorn et al. 1997a). We suspect a different origin for the filaments in NGC 1068. As is clearly apparent in Figure 1, these filaments are contained within a biconical region which is roughly aligned with the nuclear outflow/jets and the optical ionization cone seen on smaller scales. Figure 2 also shows that there is a good (though not perfect) match in P.A. between the X-ray emission and the optical filaments on large scale. This biconical geometry on small and large scales strongly suggests that the AGN is responsible for the ionization of the gas on both scales.

The large $[\text{O III}]/\text{H}\alpha$ ratios ($\gtrsim 1$; Fig. 1) observed in the gas within the large-scale cones seem to support this scenario (i.e. the hard radiation field from the AGN contributes to the high ionization level of the gas in this region). Deep MSSSO and AAT long-slit spectra of the north-east filament at $R \approx 6 - 11 \text{ kpc}$ confirm the role of the AGN. The line ratios measured along this filament are plotted in Figure 3. Using the diagnostic tools of Veilleux & Osterbrock (1987), we find that most of the line ratios are Seyfert-like. No obvious systematic gradient in the line ratios is detected along the brighter portion of the filament. The $\sim 100 \text{ km s}^{-1}$ blueshift and slight velocity gradient

apparent in the data (particularly in the higher S/N data obtained at MSSSO; see Fig. 4) are consistent with gas in rotation in the $\text{P.A.} \approx 79^\circ$ galactic disk (e.g., Galletta & Recillas-Cruz 1982; Kaneko et al. 1992; Sofue 1997; Sofue et al. 1999). The narrow line widths in the brighter portion of the filament ($\text{FWHM} < 200 \text{ km s}^{-1}$) suggest that quiescent gas from the disk is being photoionized by the central AGN. The apparent broadening in the emission-line profiles extracted from the fainter (southern) portion of the filament ($\text{FWHMs} \approx 300 - 400 \text{ km s}^{-1}$ in some locations and maybe accompanied by line splitting; see Fig. 4) may indicate that shocks become important or the AGN is photoionizing a spray of gas with a broader range of line-of-sight velocities. The elevated $[\text{N II}]/\text{H}\alpha$ and $[\text{S II}]/\text{H}\alpha$ ratios in this region (not shown in Fig. 3 because $[\text{O III}]/\text{H}\beta$ is poorly constrained) could be due to either shocks or AGN photoionization with low ionization parameter (= ratio of the density of ionizing photons to that of electrons). Intervening disk material may explain the slightly fainter emission in the south-west cone since the radiation field emerges above the disk in the north-east quadrant and below the disk in the south-west quadrant (e.g., Cecil et al. 1990; Bland-Hawthorn et al. 1997b).

3.2. NGC 1365

NGC 1365 is a giant barred Sb galaxy in the Fornax cluster, host to a beautiful grand design spiral structure and a Seyfert 1.5 nucleus. It has been the subject of several spectroscopic studies, including the pioneering work of Burbidge & Burbidge (1960) who were the first to point out the possibility of a large-scale outflow in this object. Line splitting of the $[\text{O III}]$ profiles observed by Phillips et al. (1983) and Jörsäter, Lindblad, & Bokkenberg (1984) confirmed the complex velocity field of the gas in the nuclear region, and revealed the highly ionized state of the outflowing material. Subsequent studies have traced the extent and geometry of the highly ionized outflowing material (e.g., Edmunds et al. 1988; Storchi-Bergmann & Bonatto 1991; Hjelm & Lindblad 1996; Kristen et al. 1997). An accelerated outflow in a hollow biconical structure with opening angle $\sim 100^\circ$ has been suggested (Hjelm & Lindblad 1996). This structure is roughly aligned with a jet-like radio feature observed by Sandqvist, Jörsäter, & Lindblad (1995) and Morganti et al. (1999).

TTF $\text{H}\alpha$, $[\text{N II}] \lambda 6583$, and $[\text{O III}] \lambda 5007$ images were obtained of NGC 1365; they are presented in Figures 5 – 8. The $[\text{O III}]$ data confirm the presence of the bright south-east plume of $[\text{O III}]$ -emitting material seen in previous studies, but also show for the first time fainter plumes of material on the opposite side of the nucleus. The fainter $[\text{O III}]$ emission in the TTF data extends over $\sim 1'$, and is much less conical than the bright SE plume. The $[\text{O III}] \lambda 5007/\text{H}\alpha$ ratios in this region are larger than unity, suggesting photoionization by the AGN. Strings of bright H II regions and complex dust lanes bisect the $[\text{O III}]$ structure and lowers the $[\text{O III}]/\text{H}\alpha$ ratios along a diagonal line passing immediately north of the nucleus.

The $[\text{N II}]/\text{H}\alpha$ line ratio maps shown in Figures 6 and 8 indicate that the zone of influence of the AGN in NGC 1365 extends further than suspected. $[\text{N II}] \lambda 6583/\text{H}\alpha$ ratios in excess of unity are seen out to $\sim 1'$ ($\sim 5 - 6 \text{ kpc}$) from the nucleus. Surprisingly, the high- $[\text{N II}]/\text{H}\alpha$ region appears to be almost rectangular rather than biconical, although the axis of symmetry is the same as that of the high $[\text{O III}]/\text{H}\alpha$ structure ($\text{P.A.} \approx -45^\circ$). It is not clear at present whether this fainter material is also taking place in the bright outflow studied by Hjelm

& Lindblad (1996), or is simply ambient disk material being illuminated by the central AGN.

3.3. NGC 1482

The results from our TTF imaging and optical long-slit spectroscopy of NGC 1482 have already been published in Veilleux & Rupke (2002). These data reveal a starburst-driven wind extending 1.5 kpc above and below the disk of the host galaxy with expansion velocities on the order of $\sim 250 \text{ km s}^{-1}$ and kinetic energy of at least $2 \times 10^{53} \text{ ergs}$. The TTF data are presented again in Figure 9. The $[\text{N II}] \lambda 6583/\text{H}\alpha$ ratio map derived from these data shows that the entrained wind material has $[\text{N II}] \lambda 6583/\text{H}\alpha$ ratios in excess of unity while the disk material is characterized by H II region-like line ratios indicative of the starburst. Shock ionization is suspected to be responsible for the LINER-like line ratios of the entrained material.

The new X-ray map presented in Figure 9 brings credence to this scenario. This map is based on the unpublished archived 28.56 ks exposure (P.I. D. Strickland) with the ACIS-S3 detector on the *Chandra X-ray Observatory*. High-background data were filtered out of the original image; the effective exposure time is 24.40 ks. A fixed Gaussian kernel with $\sigma = 3$ pixels ($1.5''$) was used for smoothing. The energy range of the data is 0.2 – 3 keV. The X-ray emission (especially at low energies) is elongated along the minor axis of the galaxy and shows a remarkably good match with some of the extraplanar optical filaments. A tight spatial correlation between X-ray emitting material and optical emission-line gas is also observed in two other well-known galactic winds studied in detail with *Chandra*: NGC 253 (Strickland et al. 2000) and NGC 3079 (Cecil et al. 2001; Cecil, Bland-Hawthorn, & Veilleux 2002a). In both of these cases, the data suggest that the superwind has driven cool disk gas into the halo, with X-rays being emitted either as upstream, standoff bow shocks or by cooling at cloud/wind conductive interfaces. The same phenomenon appears to be taking place in NGC 1482 (and NGC 6240; see §3.6). Good correlations between extraplanar $\text{H}\alpha$ and X-ray emission have been known to exist in a number of star-forming galaxies (e.g., Dahlem et al. 2003 and references therein), but the new *Chandra* data now show that this correlation extends down to $\sim 1''$ scale.

Reprocessing of the TTF data now reveals that the galactic wind in this galaxy extends much further than first suspected by Veilleux & Rupke (2002; see Fig. 10). The summed $\text{H}\alpha + [\text{N II}] \lambda 6583$ image now clearly shows the presence of a filament that extends out to ~ 7 kpc north-west of the nucleus. Another filament extending out to ~ 11 kpc north-east of the nucleus is visible in Figure 10, although scattered light from a bright star in the field makes the detection of this filament uncertain. Diffuse emission near the detection limit of our data also appears to be present ~ 10 kpc south of the nucleus. A high-velocity ($\sim +400 \text{ km s}^{-1}$) emission-line knot located ~ 3 kpc north of the nucleus is also visible in $[\text{N II}] \lambda 6583$ in the AAT long-slit spectrum (Fig. 11; this knot is also present at $\text{H}\alpha$ but is near the detection limit of the data). The discovery of these knots and filaments will necessarily increase the energetics involved in the outflow, although the kinematics of the gas on large scale are not yet fully constrained.

3.4. NGC 1705

NGC 1705 is a blue compact dwarf (BCD) galaxy located at 6.2 Mpc (Meurer et al. 1995). It is host to a starburst-driven

wind which is responsible for the multiple emission-line loops and arcs seen out to the Holmberg radius, ~ 2.1 kpc (Meurer et al 1992; Hunter, Hawley, & Gallagher 1993). Line splitting indicative of expansion velocities of order $\sim 100 \text{ km s}^{-1}$ is seen over most of the line-emitting gas (e.g., Meurer et al. 1992; Marlowe et al. 1995). The detection of blueshifted UV absorption lines has confirmed the presence of the wind in this object (Heckman & Leitherer 1997; Sahu & Blades 1997). Recent *FUSE* far-UV spectroscopy has revealed outflowing coronal-phase gas at a few $\times 10^5 \text{ K}$, possibly created at the interface of the warm ($\sim 10^4 \text{ K}$) optical line-emitting material and the hot outrushing gas in a blownout superbubble (Heckman et al. 2001).

The line-emitting loops and arcs seen by previous authors are easily detected with the TTF in both $\text{H}\alpha$ and $[\text{N II}] \lambda 6583$ (Fig. 12). Surprisingly, the $[\text{N II}]/\text{H}\alpha$ ratio map shows very little structure across these structures. The $[\text{N II}] \lambda 6583/\text{H}\alpha$ line ratio peaks at a value of ~ 0.3 near the location of the bright central star cluster (indicated by an arrow in Fig. 12; this star cluster is NGC 1705-1 in the nomenclature of Melnick, Moles, & Terlevich 1985). $[\text{N II}]/\text{H}\alpha$ generally stays below ~ 0.1 across the remainder of the line-emitting nebula, except perhaps in a few features where the S/N is low and the line ratio less reliable.

This line ratio map is very different from that of NGC 1482, even though both objects host similar starburst-driven winds. As discussed in the previous section, the large $[\text{N II}]/\text{H}\alpha$ ratios detected in the outflowing gas of NGC 1482 are almost certainly due to shock excitation. The fact that we do not detect significant enhancement in the $[\text{N II}]/\text{H}\alpha$ map of NGC 1705 may be due to the fact that the expansion velocities in this dwarf galaxy are considerably smaller than in NGC 1482, so that shock excitation ($\propto v_{\text{shock}}^3$) is less important than photoionization by the starburst itself. This result emphasizes an important limitation of the excitation technique suggested by Veilleux & Rupke (2002) to search for galaxies with starburst-driven winds: the results from this search technique will necessarily be biased toward powerful, shock-excited wind structures which show a sharp contrast in excitation properties relative to the star-forming hosts. Winds in dwarf galaxies will be harder to detect with this technique.

3.5. NGC 4388

NGC 4388 is a well-known Seyfert 2 galaxy located near the center of the Virgo cluster (e.g., Phillips & Malin 1982). The AGN is responsible for driving a loosely collimated outflow out of the disk of this edge-on galaxy, visible in the radio (Stone, Wilson, & Ward 1988; Hummel & Saikia 1991; Kukula et al. 1995; Falcke, Wilson, & Simpson 1998; Irwin, English, & Sorathia 1999) and optical (e.g., Veilleux et al. 1999 and references therein). A recent *Chandra* study of NGC 4388 by Iwasawa et al. (2003) now shows direct support for the galactic outflow in the X-rays. Their map is reproduced in Figure 13 along with the $\text{H}\alpha$ and $[\text{N II}] \lambda 6583$ images obtained with the TTF. Note in Table 3 that the TTF was tuned to a wavelength of 6605 Å near the nucleus of the galaxy – 13 Å below the wavelength of $\text{H}\alpha$ at systemic velocity – to map the blueshifted gas complex north of NGC 4388. Part of the soft X-ray emission is clearly produced in the disk, while the extraplanar emission is directly associated with the outflowing line-emitting material. This material is highly ionized and therefore presents only modest $[\text{N II}]/\text{H}\alpha$ ratios ($\lesssim 0.7$; Pogge 1988b; Colina 1992; Petitjean & Durret 1993).

A recent study by Yoshida et al. (2002) has revealed emission-line filaments extending out to ~ 35 kpc from the center of NGC 4388. Although the origin of these filaments is still uncertain, stripping of the interstellar medium of NGC 4388 by the ram pressure of the Virgo intracluster medium is likely to be responsible for some of these features (see also Veilleux et al. 1999). The recent discoveries of an isolated H II region and extended H I gas in the vicinity of NGC 4388 by Gerhard et al. (2002) and Vollmer & Huchtmeier (2003) bring additional support to the ram-pressure stripping scenario. The wide field of view of the TTF allows us to confirm the detection of the filaments (Fig. 14) and provide additional information on the excitation and kinematics of the line-emitting material. The [N II]/H α ratios in the brighter line-emitting knots beyond a galactocentric distance of ~ 7 kpc stay below ~ 0.7 but show no obvious monotonic gradient with distance (Fig. 15). These line ratios do not allow us to identify unambiguously the source of ionization of the gas (low-velocity shocks, AGN with low ionization parameter, or in-situ hot stars), but indicate that the ionization and excitation properties of the brighter line-emitting knots at these large distances are affected by complex variations in the ionization parameter or shock velocity rather than only the distance from the nucleus. The fact that nearly all of the emission features seen in the data of Yoshida et al. (2002) are also detected in our (slightly blueshifted) TTF images suggests that most of these features have velocities $\lesssim +100$ km s $^{-1}$ near the nucleus of the galaxy and $\lesssim +250$ km s $^{-1}$ in the outer filaments.

3.6. NGC 6240

NGC 6240 is often considered the archetype of luminous infrared galaxies ($\log[L_{\text{IR}}/L_{\odot}] = 11.8$); it has been studied thoroughly at all wavelengths. NGC 6240 is an early merger with two nuclei separated by $\sim 1''.8$ or ~ 1.28 kpc (e.g., Carral, Turner, & Ho 1990; Beswick et al. 2001; Fried & Schultz 1983; Keel 1990; Bland-Hawthorn, Wilson, & Tully 1991; Tacconi et al. 1999; Scoville et al. 2000; Tezca et al. 2000). Unambiguous signs of an AGN in this system have been detected in the hard X-rays (Iwasawa & Comastri 1998; Vignati et al. 1999). Recent high-resolution images obtained with *Chandra* show that both nuclei are X-ray emitters (Lira et al. 2002) and that both appear to be AGN (Komossa et al. 2003). Surrounding the nuclei is a large-scale soft X-ray nebula possibly powered by a superwind (Schulz et al. 1998; Komossa, Schulz, & Greiner 1998; Kłłaczyk & Dixon 2000). Signs for a superwind are also seen at optical wavelengths in the form of a complex of line-emitting filaments and arcs extending over 50×60 kpc (Heckman, Armus, & Miley 1987) and often showing violent gas motion and LINER-like line ratios (e.g., Heckman et al. 1987; Heckman, Armus, & Miley 1990; Keel 1990).

Deep H α and [N II] $\lambda 6583$ images of this object were obtained with the TTF (Figs. 16 and 17). H α emission is detected over an area $\sim 70 \times 80$ kpc centered on the nuclei. The distribution of the [N II] emission differs considerably from that of H α . The incomplete loop and filament located at P.A. $\approx 265 - 275^\circ$ and $R \approx 15 - 25$ kpc are clearly detected in the [N II] image but are hardly visible in H α ; these features have $[\text{N II}] \lambda 6583/\text{H}\alpha \gtrsim 1.4$ and stand out in the excitation map shown in Figure 16. This large-scale, high-[N II]/H α structure is roughly aligned with a 5-kpc X-ray loop detected by Komossa et al. (2003). Figure 17 also shows that the brighter portion of this loop coincides with a emission-line knot with strongly enhanced (> 1) LINER-like

[N II]/H α line ratios. These results bring further support to the galactic outflow scenario. The line-emitting gas is entrained in the starburst-driven wind. Shocks associated with the interaction between the fast wind and the slow-moving ambient gas contribute to the heating and ionization of the line-emitting material. The good match between optical line emission and X-ray emission suggests once again (see §3.3 and references therein) that the X-rays from this galactic wind are produced either by cooling at the conductive interfaces between the line-emitting clouds and the wind or as upstream, standoff bow shocks.

3.7. NGC 7213

NGC 7213 is a nearby (22.0 Mpc; $H_0 = 75$ km s $^{-1}$ Mpc $^{-1}$; Tully 1988) face-on Sa galaxy which is host to a bright Seyfert 1 nucleus with broad H α and strong hard X-ray emission (e.g., Phillips 1979; Filippenko & Halpern 1984). The nuclear spectrum also exhibits narrow LINER-like emission lines produced by the diffuse gas around the Seyfert nucleus. Figure 18 shows deep H α and [N II] $\lambda 6583$ images of this object obtained with the TTF. The TTF data recover the ring of H II regions known to exist around the bright active nucleus of this galaxy (Storchi-Bergmann et al. 1996). The TTF image also reveals the presence of a line-emitting filament located ~ 19 kpc from the nucleus, well outside the optical radius of this galaxy. This filament was independently discovered by Hameed et al. (2001), who argues that it is the ionized portion of tidal debris from a recent merger.

The TTF data suggest that the [N II]/H α ratios in the filament are unlike those typically seen in H II regions (e.g., ring of H II regions near the nucleus). The line ratios measured from a deep long-slit spectrum obtained with the MSSSO 2.3-meter telescope confirm this result and indicate that the emission in the filament is LINER-like, based on the locations of the line ratios in diagnostic diagrams (Fig. 19). Dilute photoionization by a faint and distant AGN with ionization parameter $\log U \approx -3$ (i.e. the density of ionizing photon is 10^{-3} that of electron) could explain these line ratios (e.g., Ferland & Netzer 1983), although shock ionization cannot be formally excluded (Dopita & Sutherland 1995).

The kinematics of this filament can be used to distinguish between these two scenarios. Multi-line imaging slightly shifted in velocity space suggests that the line-emitting gas is blueshifted by $\sim 150 - 200$ km s $^{-1}$ with respect to systemic velocity. The MSSSO spectrum of the filament confirms this small blueshift (Fig. 20). These measurements indicate that the optical filament coincides not only spatially with the H I feature of Hameed et al. (2001) but also kinematically. Moreover, the narrow line widths ($\sim 80 - 200$ km s $^{-1}$) measured in the optical filament indicate that the gas must not be affected significantly by shocks. This strongly suggests that the line-emitting filament simply represents tidal debris which are being ionized by the AGN in NGC 7213. Only a small fraction of the H I tidal complex is visible in H α because the radiation field from NGC 7213 is not isotropic. According to the unified model of Seyfert galaxies, our line of sight to the Seyfert 1 nucleus has to lie within the opening angle of the inner torus/accretion disk. Given the face-on orientation of the host galaxy, this would imply that both our line of sight and the line-emitting filament lie within the ionizing cone of the accretion disk and above the galactic disk of NGC 7213.

3.8. Circinus Galaxy

The Circinus galaxy (Freeman et al. 1977) is host to a well-known ionization cone and large-scale outflow visible in the radio (e.g., Elmouttie et al. 1998a), optical (e.g., Marconi et al. 1994; Lehnert & Heckman 1995; Veilleux & Bland-Hawthorn 1997; Elmouttie et al. 1998b; Wilson et al. 2000), near-infrared (Maiolino et al. 1998; Ruiz et al. 2000), and X-rays (Sambruna et al. 2001a, 2001b; Smith & Wilson 2001). The source of the ionization and outflow appears to be the central Seyfert nucleus, although a circumnuclear starburst is also present in this object (e.g., Veilleux & Bland-Hawthorn 1997; Elmouttie et al. 1998b).

A new TTF [O III] $\lambda 5007$ image of the Circinus galaxy is presented in Figure 21. This image reaches fainter flux levels than the Fabry-Perot data presented in Veilleux & Bland-Hawthorn (1997). The new data confirm the presence of the bright high-ionization filaments within 0.5 kpc of the nucleus. But the deeper TTF image also reveals unsuspected [O III] emission which extends ~ 1 kpc west and north-west of the nucleus. Very faint, filamentary emission appears to extend out to ~ 1.2 kpc from the nucleus along P.A. $\approx 315^\circ$, but this needs to be confirmed with deeper images. The TTF image also shows a few additional knots of emission in the northern/northwestern quadrant and to the south. The southernmost of these features appears to coincide with *Chandra* source F in Smith & Wilson (2001), located ~ 500 pc due south from the nucleus. This is shown in the lower left panel of Figure 21, where the *Chandra* data are superposed on the TTF [O III] image.

3.9. ESO484-G036

ESO484-G036 is an edge-on Sb galaxy from the *IRAS* Bright Galaxy Sample (Soifer et al. 1989; F04335–2514). The optical classification of the nucleus of this galaxy is ambiguous due to weak H β and [O III] emission (Kim et al. 1995; Veilleux et al. 1995). Long-slit spectroscopy by Lehnert & Heckman (1995) indicates the presence of large positive gradients in [N II]/H α , [S II]/H α and [O I]/H α along the minor axis of this galaxy. Conventional H α + [N II] narrowband imaging of this object by these same authors reveals a cross-like structure aligned along the major and minor axes of the disk.

The TTF data confirm the cross-like morphology of the line emission in ESO484-G036 (especially visible in [N II]; Fig. 22). The [N II]/H α ratio map also confirms the steep excitation gradient along the minor axis of the galaxy. The disk emission presents a H II region-like [N II]/H α ratios of ~ 0.5 (but note that [N II]/H α reaches a minimum ~ 1 kpc south-west of the nucleus), while the emission 1 kpc above and below the disk have [N II]/H α that are in the range ~ 1 –2.4. This line ratio map is reminiscent of that of NGC 1482, but the larger distance of ESO484-G036 (~ 60 Mpc instead of 20 Mpc for NGC 1482) makes the extraplanar emission more difficult to resolve in this object. The new TTF data add strong support to the idea that ESO484-G036 is indeed host to a starburst-driven wind (Lehnert & Heckman 1996), and also show the promise of using excitation maps for systematic searches for starburst-driven winds in the local universe (Veilleux & Rupke 2002).

3.10. MR 2251–178

In the course of our TTF study, the radio-quiet quasar MR 2251–178 was imaged at H α . This is the most distant ($z = 0.064$) object in the sample. The results on this object have already been published by Shopbell, Veilleux, & Bland-Hawthorn (1999); the TTF images are reproduced for the sake

of completeness in Figure 23. The TTF data reveal a very extended nebula centered on and photoionized by this quasar. The spiral-like complex is seen extending more or less symmetrically over ~ 200 kpc. Narrow-band images obtained at slightly different wavelengths reveal a large-scale rotation pattern which is in the opposite sense as that seen in the inner region of the galaxy (see also Bergeron et al. 1983; Nørgaard-Nielsen et al. 1986). As discussed in detail in Shopbell et al., the large and symmetric morphology of the gaseous envelope and its smooth large-scale rotation suggest that the envelope did not originate with a cooling flow, a past merger event, or an interaction with any of the galaxies in the field. Shopbell et al. favor a model in which the extended ionized nebula resides within a large complex of H I gas centered on the quasar. Slightly blueshifted (~ 300 km s $^{-1}$) UV and warm X-ray absorbers are seen in HST and ASCA/ROSAT spectra of MR 2251–178 (Reynolds 1997; Komossa 2001; Monier et al. 2001; Ganguly, Charlton, & Eracleous 2001), but they are presumed to arise from nuclear material near the AGN rather than from gas extending on galactic scale. An error of a factor of 2.25 was recently found in the flux calibration of the TTF data. All fluxes listed in Shopbell et al. (1999) should be scaled down by this factor. This correction does not affect the conclusions of the paper.

4. DISCUSSION AND FUTURE AVENUES OF RESEARCH

We have presented the results from a deep emission-line imaging survey of 10 nearby starburst and active galaxies using the TTF on the AAT and WHT. The topology and projected cross-section of the line-emitting gas varies widely among the galaxies in the sample. Very large ($\gtrsim 80$ kpc) ionized complexes are discovered around NGC 6240 and MR 2251–178. Emission-line knots and wispy filaments are confirmed to be present in the halo of NGC 4388 at distances of up to ~ 30 kpc from the active nucleus. Diffuse and filamentary gas associated with large-scale (10–20 kpc) ionization cones or outflows are detected for the first time in NGC 1068, NGC 1365, and NGC 1482 and confirmed in NGC 7213. Emission-line structures on \gtrsim kpc scale are revealed in the galactic winds of NGC 1705, Circinus galaxy, and ESO484-G036.

Multi-line imaging and long-slit spectroscopy of the gas found on large scale reveal line ratios which are generally not H II region-like. Shocks often contribute significantly to the ionization of the outflowing gas on the outskirts of starburst galaxies. As expected from shock models (e.g., Dopita & Sutherland 1995), the importance of shocks over photoionization by OB stars appears to scale with the velocity of the outflowing gas (e.g., NGC 1482, NGC 6240, or ESO484-G036 versus NGC 1705; NGC 3079 is an extreme example of a shock-excited wind nebula; Veilleux et al. 1994), although other factors like the starburst age, star formation rate, and the dynamical state of the outflowing structure (e.g., pre- or post-blowout) must also be important in determining the excitation properties of the gas at these large radii (e.g., see discussion in Shopbell & Bland-Hawthorn 1998 and Veilleux & Rupke 2002). When an active nucleus is present, the radiation field from the AGN appears to be the primary source of ionization for the filaments within ~ 10 –20 kpc of the nucleus, but the impact of the AGN tapers off at larger distances (e.g., $\gtrsim 30$ kpc in NGC 4388), unless the source of radiation is a powerful quasar (MR 2251–178).

Given the small sample size and methods of selection of the

sample, no statistical statement can be made on the frequency of occurrence of large-scale nebulae around starburst and active galaxies in general. The objects in our sample were specifically selected to host ionization cones and/or galactic winds on \sim kpc scale. The high discovery rate of $\gtrsim 10$ -kpc nebulae in our sample may not be typical of the local population of starburst and active galaxies. It is also not clear at present whether the power and type of AGN (type 1 *versus* type 2) is important in determining the amount of ionized gas detectable with the TTF. In the matter-bounded scenario (e.g., infinite reservoir of H I gas surrounding the active nucleus in all directions), one would expect a correlation between AGN ionizing power and the detected mass of ionized material – this may be why the largest nebula is found around the most powerful AGN in our sample (MR 2251–178). In this simple scenario, the orientation of the AGN accretion disk to our line of sight (nearly face-on in type 1s *versus* nearly edge-on in type 2s) should to first order determine the geometry of the ionized material: biconical in Seyfert 2s (e.g., NGC 1068) and more isotropic in Seyfert 1s (e.g., MR 2251–178; see detailed predictions in Mulchaey, Wilson, & Tsvetanov 1996). However, this simple scenario clearly does not apply to all AGNs in our sample (e.g., NGC 7213). The topology and projected cross-section of the warm ionized gas in AGN necessarily also depend on the properties of the host galaxy (e.g., morphological type, gas content) and immediate environment (e.g., presence of a tidal complex as in the case of NGC 7213).

Our pilot survey raises similar questions for starburst galaxies. There is a clear need to expand the starburst sample to look for possible dependence on the age and power of the starburst and the dynamical state of the outflow. These data will provide the material to test the idea of using excitation maps (e.g., [N II]/H α) to detect superwind galaxies (Veilleux & Rupke 2002). If found to be successful at low redshifts, this method could be used in the future to more efficiently identify distant galaxies hosting powerful starburst-driven winds.

The advent of tunable filters on 8-meter class telescopes [e.g., OSIRIS on the GranTeCan (Cepa et al. 2000) and the Maryland-Magellan Tunable Filter on the Baade 6.5-m telescope] should improve the sensitivity of emission-line galaxy surveys at least tenfold. Measurements with this second generation of tunable filters will provide direct quantitative constraints on the gaseous cross-section of active and star-forming galaxies, and the importance of mass exchange between galaxies and their environment. The detection of warm ionized complexes that extend several tens of kpc over wide opening angles would make them likely candidates for the higher column density Ly α cloud population detected in quasar spectra (e.g., Bergeron et al. 1994; Lanzetta et al. 1995; Norman et al. 1996; Steidel et al. 2002). The kinematic information derived from these data will constrain the origin of the gas: is it taking part in an outflow or is it an extension of the HI disk, remnant accreting gas from galaxy formation, or debris from a recent galaxy interaction or ram-pressure stripping episode?

We are grateful to E. Brinks for providing the H I map of NGC 1068 prior to publication and to K. Iwasawa and A. Wilson for the *Chandra* X-ray data of NGC 4388. We thank the referee, Matthias Ehle, for constructive comments. This article was written while S.V. was on sabbatical at the California Institute of Technology and the Observatories of the Carnegie Institution of Washington; S.V. thanks both of these institutions for their hospitality. S.V. acknowledges partial support of this research by a Cottrell Scholarship awarded by the Research Corporation, NASA/LTSA grant NAG 56547, and NSF/CAREER grant AST-9874973. D.S.R. was also supported in part by NSF/CAREER grant AST-9874973. This research has made use of the NASA/IPAC Extragalactic Database (NED), which is operated by the Jet Propulsion Laboratory, California Institute of Technology, under contract with the National Aeronautics and Space Administration.

REFERENCES

- Adelberger, K. L., Steidel, C. C., Shapley, A. E., & Pettini, M. 2003, ApJ, 584, 45
- Antonucci, R. R. J., & Miller, J. S. 1985, ApJ, 297, 621
- Arribas, S., Mediavilla, E., & Garcia-Lorenzo, B. 1996, ApJ, 463, 509
- Bajtlik, S., Duncan, R. C., & Ostriker, J. P. 1988, ApJ, 327, 570
- Baldwin, J., Wilson, A. S., & Whittle, M. 1987, ApJ, 319, 84
- Bergeron, J., Boksenberg, A., Dennefeld, M., & Tarenghi, M. 1983, MNRAS, 202, 125
- Bergeron, J., et al. 1994, ApJ, 436, 33
- Beswick, R. J., Pedlar, A., Mundell, C. G., & Gallimore, J. F. 2001, MNRAS, 325, 151
- Bland-Hawthorn, J. 1999, Nature, 400, 220
- Bland-Hawthorn, J., Freeman, K. C., & Quinn, P. J. 1997a, ApJ, 490, 143
- Bland-Hawthorn, J., Lumsden, S. L., Voit, G. M., Cecil, G. N., & Weisheit, J. C. 1997b, Ap&SS, 248, 177
- Bland-Hawthorn, J., & Jones, D. H. 1998, PASA, 15, 44
- Bland-Hawthorn, J., & Kedziora-Chudczer, L. 2003, PASA, in press (astro-ph/0305032)
- Bland-Hawthorn, J., Lumsden, S. L., Voit, G. M., Cecil, G. N., & Weisheit, J. C. 1997, Ap&SS, 248, 177
- Bland-Hawthorn, J., Sokolowski, J., & Cecil, G. 1991, ApJ, 375, 78
- Bland-Hawthorn, J., Veilleux, S., Cecil, G. N., Putman, M. E., Gibson, B. K., & Maloney, P. R. 1998, MNRAS, 299, 611
- Bland-Hawthorn, J., Wilson, A. S., & Tully, R. B. 1991, ApJ, 371, L19
- Blitz, L., Spergel, D. N., Teuben, P. J., Hartmann, D., Burton, W. B. 1999, ApJ, 514, 818
- Böhringer, H., Voges, W., Fabian, A. C., Edge, A. C., & Neumann, D. M. 1993, MNRAS, 264, L25
- Burbidge, E. M., & Burbidge, G. R. 1960, ApJ, 132, 30
- Carra, P., Turner, J. L., & Ho, P. T. P. 1990, ApJ, 362, 434
- Cecil, G., Bland, J., & Tully, R. B. 1990, ApJ, 355, 70
- Cecil, G., Bland-Hawthorn, J., Veilleux, S., & Filippenko, A. V. 2001, ApJ, 555, 338
- Cecil, G., Bland-Hawthorn, J., & Veilleux, S. 2002a, ApJ, 576, 745
- Cecil, G., et al. 2000, ApJ, 536, 675
- Cecil, G., et al. 2002b, ApJ, 568, 627
- Cepa, J., et al. 1990, in Optical and IR Telescope Instrumentation and Detectors, eds. M. Iye and A. F. Moorwood, Proc. SPIE, 4008, 623
- Colina, L. 1992, ApJ, 386, 59
- Crenshaw, D. M., & Kraemer, S. B. 2000, ApJ, 532, L101
- Dahlem, M., Ehle, M., Jansen, F., Heckman, T. M., Weaver, K. A., Strickland, D. K. 2003, A&A, 403, 547
- Dahlem, M., Lazendic, J. S., Haynes, R. F., Ehle, M., Lisenfeld, U. 2001, A&A, 374, 42
- Dahlem, M., Petr, M. G., Lehnert, M. D., Heckman, T. M., Ehle, M. 1997, A&A, 320, 731
- de Vaucouleurs, G., de Vaucouleurs, A., Corwin, H. G. Jr., & Buta, R. J., Paturel, G., & Fouqué, P. 1991, Third Reference Catalogue of Bright Galaxies (New York, Springer-Verlag)
- Devine, D., & Bally, J. 1999, ApJ, 510, 197
- Dopita, M. A., Groves, B. A., Sutherland, R. S., Binette, L., & Cecil, G. 2002, ApJ, 572, 753
- Dopita, M. A., & Sutherland, R. S. 1995, ApJ, 455, 468
- Edmunds, M. G., Taylor, K., & Turtle, A. J. 1988, MNRAS, 234, 155
- Elmouttie, M., Haynes, R. F., Jones, K. L., Sadler, E. M., & Ehle, M. 1998a, MNRAS, 297, 1202
- Elmouttie, M., et al. 1998b, MNRAS, 297, 49
- Fabian, A. C., et al. 2000, MNRAS, 318, L65
- Fabian, A. C. 2001, MNRAS, 321, L20
- Falcke, H., Wilson, A. S., & Simpson, C. 1998, ApJ, 502, 199
- Ferguson, A., van der Hulst, T., & van Gorkom, J. 2001, AAO Newsletter, 96, 4
- Ferland, G. J., & Netzer, H. 1983, ApJ, 264, 105

- Filippenko, A. V., & Halpern, J. P. 1984, *ApJ*, 285, 458
- Frantz, M., & Illingworth, G. 1990, *ApJ*, 359, L41
- Freeman, K. C., et al. 1977, *A&A*, 55, 445
- Fried, J. W., & Schulz, H. 1983, *A&A*, 118, 166
- Fukugita, M., Hogan, C. J., & Peebles, P. J. E. 1998, *ApJ*, 503, 518
- Galletta, G., & Recillas-Cruz, E. 1982, *A&A*, 112, 361
- Gallimore, J., et al. 1996, *ApJ*, 464, 198
- Ganguly, R., Charlton, J. C., & Eracleous, M. 2001, *ApJ*, 556, L7
- Gerhard, O., Arnaboldi, M., Freeman, K. C., & Okamura, S. 2002, *ApJ*, 580, L121
- Glazebrook, K., & Bland-Hawthorn, J. 2001, *PASP*, 113, 197
- Hameed, S., Blank, D. L., Young, L. M., & Devereux, N. 2001, *ApJ*, 546, L97
- Heckman, T. M., Armus, L., & Miley, G. K. 1987, *AJ*, 93, 276
- . 1990, *ApJS*, 74, 833
- Heckman, T. M., & Leitherer, C. 1997, *AJ*, 114, 69
- Heckman, T. M., et al. 2001, *ApJ*, 554, 1021
- Heinz, S., Choi, Y.-Y., Reynolds, C. S., & Begelman, M. C. 2002, *ApJ*, 569, L79
- Helfer, T. T., & Blitz, L. 1995, *ApJ*, 450, 90
- Hjelm, M., & Lindblad, P. O. 1996, *A&A*, 305, 727
- Hummel, E., & Saikia, D. J. 1991, *A&A*, 249, 43
- Hunter, D. A., Hawley, W. N., & Gallagher, J. S. III 1993, *AJ*, 106, 1797
- Irwin, J. A., English, J., & Sorathia, B. 1999, *AJ*, 117, 2102
- Iwasawa, K., & Comastri, A. 1998, *MNRAS*, 297, 1219
- Iwasawa, K., Wilson, A. S., Fabian, A. C., & Young, A. J. 2003, *MNRAS*, submitted
- Jenkins, A., et al. 1998, *ApJ*, 499, 20
- Jörsäter, S., Lindblad, P. O., & Boksenberg, A. 1984, *A&A*, 140, 288
- Jones, D. H., Shopbell, P. L., & Bland-Hawthorn, J. 2002, *MNRAS*, 329, 759
- Kaneko, N., et al. 1992, *AJ*, 103, 422
- Keel, W. C. 1990, *AJ*, 100, 356
- Kim, D.-C., Sanders, D. B., Veilleux, S., Mazzarella, J. M., & Soifer, B. T. 1995, *ApJS*, 98, 129
- Kinkhabwala, A., et al. 2002, *ApJ*, 575, 732
- Kolaczyk, E. D., & Dixon, D. D. 2000, *ApJ*, 534, 490
- Komossa, St. 2001, *A&A*, 367, 801
- Komossa, St., Schulz, H., & Greiner, J. 1998, *A&A*, 334, 110
- Komossa, St., et al. 2003, *ApJ*, 582, L15
- Kraemer, S. B., Ruiz, J. R., & Crenshaw, D. M. 1998, *ApJ*, 508, 232
- Kristen, H., Jörsäter, S., Lindblad, P. O., & Boksenberg, A. 1997, *A&A*, 328, 483
- Kukula, M. J., Pedlar, A., Baum, S. A., & O'Dea, C. P. 1995, *MNRAS*, 276, 1262
- Lanzetta, K. M., Bowen, D. V., Tytler, D., & Webb, J. K. 1995, *ApJ*, 442, 538
- Larson, R. B., & Dinerstein, H. L. 1975, *PASP*, 87, 911
- Lehnert, M. D., & Heckman, T. M. 1995, *ApJS*, 97, 89
- . 1996, *ApJ*, 462, 651
- Lehnert, M. D., Heckman, T. M., & Weaver, K. A. 1999, *ApJ*, 523, 575
- Lira, P., Ward, M. J., Zezas, A., & Murray, S. S. 2002, *MNRAS*, 333, 709
- Macchetto, F., Capetti, A., Sparks, W. B., Axon, D. J., & Boksenberg, A. 1994, *ApJ*, 435, L15
- Maiolino, R., Krabbe, A., Thatte, N., & Genzel, R. 1998, *ApJ*, 493, 650
- Marconi, A., Moorwood, A. F. M., Origlia, L., & Oliva, E. 1994, *Messenger*, 78, 20
- Marlowe, A. T., Heckman, T. M., Wyse, R. F. G., & Schommer, R. 1995, *ApJ*, 438, 285
- McNamara, B. R., et al. 2000, *ApJ*, 534, L135
- Melnick, J., Moles, M., & Terlevich, R. 1985, *A&A*, 149, L24
- Meurer, G. R., et al. 1999, *BAAS*, 194, 501
- Meurer, G. R., Freeman, K. C., Dopita, M. C., & Cacciari, C. 1992, *AJ*, 103, 60
- Meurer, G. R., et al. 1995, *AJ*, 110, 2665
- Miller, J. S., & Antonucci, R. R. J. 1983, *ApJ*, 271, L7
- Miller, J. S., Goodrich, R. W., & Mathews, W. G. 1991, *ApJ*, 378, 47
- Miller, S. T., & Veilleux, S. 2003a, *ApJS*, 148, 000
- . 2003b, *ApJ*, 592, 000
- Monier, E. M., Mathur, S., Wilkes, B., & Elvis, M. 2001, *ApJ*, 559, 675
- Morganti, R., Tsvetanov, Z. I., Gallimore, J., & Allen, M. G. 1999, *A&AS*, 137, 457
- Mulchaey, J. S., Wilson, A. S., & Tsvetanov, Z. 1996, *ApJ*, 467, 197
- Nörgaard-Nielsen, H. U., Hansen, L., Jørgesen, H. E., & Christensen, P. R. 1986, *A&A*, 169, 49
- Norman, C. A., Bowen, D. V., Heckman, T. M., Blades, C., & Danly, L. 1996, *ApJ*, 472, 73
- Petitjean, P., & Durret, F. 1993, *A&A*, 277, 365
- Phillips, M. M. 1979, *ApJ*, 227, L121
- Phillips, M. M., & Malin, D. F. 1982, *MNRAS*, 199, 205
- Phillips, M. M., Turtle, A. J., Edmunds, M. G., & Pagel, B. E. J. 1983, *MNRAS*, 203, 759
- Pogge, R. W. 1988a, *ApJ*, 328, 519
- . 1988b, *ApJ*, 332, 702
- Putman, M. E., Bland-Hawthorn, J., Veilleux, S., Gibson, B. K., Freeman, K. C., & Maloney, P. R. 2003, *ApJ*, submitted
- Quilis, V., Bower, R. G., & Balogh, M. L. 2001, *MNRAS*, 328, 1091
- Rauch, M. 1998, *ARA&A*, 36, 267
- Reynolds, C. J. 1997, *MNRAS*, 286, 513
- Ruiz, M., et al. 2000, *MNRAS*, 316, 49
- Sahu, M. S., & Blades, J. C. 1997, *ApJ*, 484, L125
- Sambrook, R. M., et al. 2001a, *ApJ*, 546, L9
- . 2001b, *ApJ*, 546, L13
- Sandqvist, Aa., Jörsäter, S., & Lindblad, P. O. 1995, *A&A*, 295, 585
- Schulz, H., Komossa, S., Berghöfer, T., & Boer, B. 1998, *A&A*, 330, 823
- Scoville, N. Z., et al. 2000, *AJ*, 119, 991
- Scoville, N. Z., Matthews, K., Carico, D. P., & Sanders, D. B. 1988, *ApJ*, 327, L61
- Seyfert, C. K. 1943, *ApJ*, 97, 28
- Shopbell, P. L., & Bland-Hawthorn, J. 1998, *ApJ*, 493, 129
- Shopbell, P. L., Veilleux, S., & Bland-Hawthorn, J. 1999, *ApJ*, 524, L83
- Smith, D. A., & Wilson, A. S. 2001, *ApJ*, 557, 180
- Sofue, Y. 1997, *PASJ*, 49, 17
- Sofue, Y., et al. 1999, *ApJ*, 523, 136
- Soifer, B. T., Boehme, L., Neugebauer, G., & Sanders, D. B. 1989, *AJ*, 98, 766
- Sokolowski, J., Bland-Hawthorn, J., & Cecil, G. 1991, *ApJ*, 375, 583
- Steidel, C. C., et al. 2002, *ApJ*, 576, 653
- Steidel, C. C., Pettini, M., Adelberger, K. L. 2001, *ApJ*, 546, 665
- Stevens, I. R., Read, A. M., & Bravo-Guerrero, J. 2003, *MNRAS*, preprint (astro-ph/0306334)
- Stone, J. L., Wilson, A. S., & Ward, M. J. 1988, *ApJ*, 330, 105
- Storchi-Bergmann, T., & Bonatto, C. 1991, *MNRAS*, 250, 138
- Storchi-Bergmann, T., Rodriguez-Ardila, A., Schmitt, H. R., Wilson, A. S., & Baldwin, J. A. 1996, *ApJ*, 472, 83
- Strickland, D. K., Heckman, T. M., Weaver, K. A., & Dahlem, M. 2000, *AJ*, 120, 2965
- Tacconi, L., et al. 1999, *ApJ*, 524, 732
- Tadhunter, C., Villar-Martín, M., Morganti, R., Bland-Hawthorn, J., & Axon, D. 2000, *MNRAS*, 314, 849
- Tezca, M., et al. 2000, *ApJ*, 537, 178
- Tully, R. B. 1988, *Nearby Galaxies Catalog*, Cambridge University Press
- Thronson, H. A., et al. 1989, *ApJ*, 343, 158
- Vader, P. 1986, *ApJ*, 305, 669
- Veilleux, S. 2002, in *Extragalactic Gas at Low Redshift*, ASP Conf. Proc. Vol. 254, eds. J. S. Mulchaey and J. Stocke, San Francisco: Astronomical Society of the Pacific, 313
- Veilleux, S., & Bland-Hawthorn, J. 1997, *ApJ*, 479, L105
- Veilleux, S., Bland-Hawthorn, J., Cecil, G., Tully, R. B., & Miller, S. T. 1999, *ApJ*, 520, 111
- Veilleux, S., Cecil, G., Bland-Hawthorn, J., Tully, R. B., Filippenko, A. V., & Sarger, W. L. W. 1994, *ApJ*, 433, 48
- Veilleux, S., Kim, D.-C., Sanders, D. B., Mazzarella, J. M., & Soifer, B. T. 1995, *ApJS*, 98, 171
- Veilleux, S., & Osterbrock, D. E. 1987, *ApJS*, 63, 295
- Veilleux, S., & Rupke, D. S. 2002, *ApJ*, 565, L63
- Vignati, P., et al. 1999, *A&A*, 349, L57
- Vollmer, B., & Huchthmeier, W. 2003, *A&A*, in press (astro-ph/0303531)
- Walker, M. 1968, *ApJ*, 151, 71
- Weymann, R. J., Vogel, S. N., Veilleux, S., Epps, H. W. 2001, *ApJ*, 561, 559
- Wilson, A. S., et al. 2000, *AJ*, 120, 1325
- Wilson, A. S., & Tsvetanov 1994, *AJ*, 107, 1227
- Wilson, A. S., & Ulvestad, J. 1987, *ApJ*, 319, 105
- Yoshida, M., et al. 2002, *ApJ*, 567, 118
- Young, A. J., Wilson, A. S., & Shopbell, P. L. 2001, *ApJ*, 556, 6

FIG. 1.— NGC 1068 in (a) R0 continuum, (b) H α , (c) [O III] λ 5007, and (d) [O III] λ 5007/H β ratio ($\equiv 2.85 \times$ [O III] λ 5007/H α). North is up and east to the left. The cross in each panel marks the location of the nucleus from NED. The flux scale of the emission-line maps is logarithmic, while the ratio map is on a linear scale. The flux scale for the [O III] data ranges from -17.5 to -15.0 , while the scale for the H α map ranges from -18.5 to -15.0 . Emission from both [O III] and H α is detected for the first time out to ~ 11 kpc from the nucleus in the north-east (upper left) and south-west (lower right) quadrants, roughly aligned with the ionization cone on smaller scale. Note the high [O III]/H β ratios in the large-scale filaments. The diffuse emission features at the eastern edge of panel (b) and southern edge of panel (c) are artifacts of reflective ghosts associated with the TTF.

FIG. 2.— Multiwavelength comparison in NGC 1068. (a) H α and H I 21-cm contour map (from Brinks 2003; private communication) and (b) [O III] λ 5007 and X-ray contour map from Young, Wilson, & Shopbell (2001). North is up and east to the left. The emission-line maps are on the same flux scale as in Figure 1. The contours in the HI map are at 25, 100, 150, 200, and 250 Jansky s^{-1} beam $^{-1}$. Refer to Young et al. (2001) for the values of the X-ray contour levels. The cross in each panel marks the location of the nucleus from NED. Note the slight misalignment between the large-scale filaments and the inner ionization cone defined by the X-ray emission. The diffuse emission feature at the southern edge of panel (b) is a reflective ghost associated with the TTF.

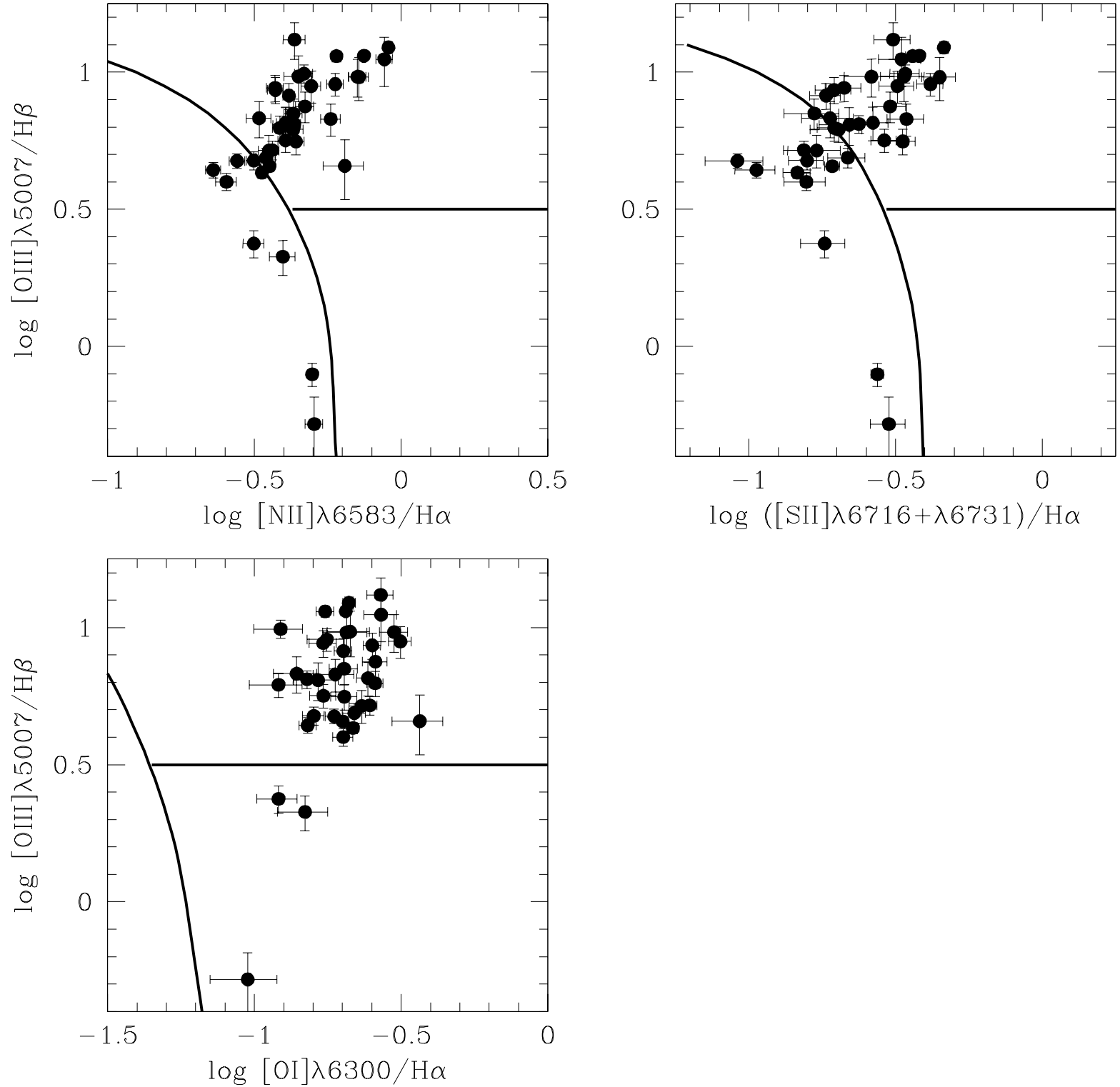


FIG. 3.— Emission-line ratios measured along the north-east filament (P.A. = 3°) located at $\sim 6 - 12$ kpc from the nucleus of NGC 1068. Most of the line ratios are Seyfert-like, therefore indicating that the filament is ionized by the central AGN.

FIG. 4.— Continuum-subtracted long-slit spectrum obtained along the north-east filament located at ~ 6 – 12 kpc from the nucleus of NGC 1068. The slit is oriented along P.A. = 3° with North at the top. The white horizontal band is hiding the spectrum of a bright star. The flux scale is logarithmic and in units of $\text{erg s}^{-1} \text{cm}^{-2}$. The velocities are relative to systemic ($= 1792 \text{ km s}^{-1}$). The blueshift, velocity gradient, and narrow line widths in the brighter portion of the filament are consistent with quiescent gas in galactic rotation. Note, however, that the emission-line profiles become broader in the fainter (southern) portion of the filament, perhaps a sign that shocks become important here or the gas ionized by the AGN spans a broader range of line-of-sight velocities.

FIG. 5.— Outer regions of NGC 1365 in (a) B4 continuum, (b) $\text{H}\alpha$, (c) $[\text{O III}] \lambda 5007$, and (d) $[\text{O III}] \lambda 5007/\text{H}\beta$ ratio ($\equiv 2.85 \times [\text{O III}] \lambda 5007/\text{H}\alpha$). North is up and east to the left. The cross in each panel marks the location of the red continuum peak. The flux scale of the emission-line maps is logarithmic, while the ratio map is on a linear scale. A ~ 7 -kpc ionization cone is visible in the ratio maps.

FIG. 6.— Outer regions of NGC 1365 in (a) R0 continuum, (b) $\text{H}\alpha$, (c) $[\text{N II}] \lambda 6583$, and (d) $[\text{N II}] \lambda 6583/\text{H}\alpha$ ratio. North is up and east to the left. The cross in each panel marks the location of the red continuum peak. The flux scale of the emission-line maps is logarithmic, while the ratio map is on a linear scale. A ~ 12 -kpc boxy region with $[\text{N II}]/\text{H}\alpha > 1$ is detected around the nucleus.

FIG. 7.— Central regions of NGC 1365 in (a) B4 continuum, (b) $\text{H}\alpha$, (c) $[\text{O III}] \lambda 5007$, and (d) $[\text{O III}] \lambda 5007/\text{H}\beta$ ratio ($\equiv 2.85 \times [\text{O III}] \lambda 5007/\text{H}\alpha$). North is up and east to the left. The cross in each panel marks the location of the red continuum peak. The flux scale of the emission-line maps is logarithmic, while the ratio map is on a linear scale. The ratio map clearly shows a ionization cone bisected by a dust lane.

FIG. 8.— Central regions of NGC 1365 in (a) R0 continuum, (b) $\text{H}\alpha$, (c) $[\text{N II}] \lambda 6583$, and (d) $[\text{N II}] \lambda 6583/\text{H}\alpha$ ratio. The contours in (d) show the $[\text{O III}] \lambda 5007/\text{H}\beta$ ratios from Fig. 7. North is up and east to the left. The cross in each panel marks the location of the red continuum peak. The flux scale of the emission-line maps is logarithmic, while the ratio map is on a linear scale. The contour levels of the $[\text{O III}]/\text{H}\beta$ ratio map are at 0.58 , 2.9 , and $9.2 \times 10^{-15} \text{ erg s}^{-1} \text{cm}^{-2} \text{arcsecond}^{-2}$. A large boxy region with $[\text{N II}]/\text{H}\alpha > 1$ is detected around the nucleus.

FIG. 9.— NGC 1482 in (a) R0 continuum, (b) $\text{H}\alpha$, (c) $[\text{N II}] \lambda 6583$ and *Chandra* X-ray contour map, and (d) $[\text{N II}] \lambda 6583/\text{H}\alpha$ ratio. North is up and east to the left. The crosses in each panel indicate the locations of the two peaks in the red continuum. The flux scale of the emission-line maps is logarithmic, while the ratio map is on a linear scale. The contour levels of the X-ray map are at 3.0 , 5.4 , 17 , and $169 \times 10^{-4} \text{ counts s}^{-1} \text{arcsecond}^{-2}$ (based on an effective exposure time of 24.40 ksec). Note the tight match between the X-ray emission and some of the optical filaments.

FIG. 10.— *Chandra* X-ray contour map superposed on a very deep $\text{H}\alpha + [\text{N II}] \lambda 6583$ image of NGC 1482. North is up and east to the left. The crosses indicate the locations of the two peaks in the red continuum. The flux scale is logarithmic. The contour levels of the X-ray map are the same as in Figure 9. Filamentary line emission is detected out to ~ 7 kpc north-west of the nucleus, and perhaps out to ~ 12 kpc to the north-east. Diffuse emission may also be present ~ 10 kpc south of the nucleus. A bright star on the eastern edge of the image was masked for display purposes; it may be responsible for reflective ghosts that can be confused with faint emission-line features.

FIG. 11.— Long-slit spectra of NGC 1482 centered on $\text{H}\alpha$ and $[\text{N II}] \lambda 6583$. The position angle of the slit in both spectra is perpendicular to the galaxy disk (North is up). In the left two panels, the slit is centered on the nucleus while it is offset $5''$ west of the nucleus in the two panels on the right. The velocities are relative to systemic ($= 1915 \text{ km s}^{-1}$). The flux scale is logarithmic to emphasize the presence of the faint emission-line knot (indicated by the black circle) at ~ 3 kpc North and $+400 \text{ km s}^{-1}$, more easily visible in $[\text{N II}]$ than at $\text{H}\alpha$.

FIG. 12.— NGC 1705 in (a) R0 continuum, (b) $\text{H}\alpha$, (c) $[\text{N II}] \lambda 6583$, and (d) $[\text{N II}] \lambda 6583/\text{H}\alpha$ ratio. North is up and east to the left. The cross in each panel marks the location of the red continuum peak. The flux scale of the emission-line maps is logarithmic, while the ratio map is on a linear scale. Note the well-known arcs and bubble-like structures in this galaxy, and the surprising lack of structure in the excitation map across these features.

FIG. 13.— Inner regions of NGC 4388 in (a) R0 continuum, (b) $\text{H}\alpha$, (c) $[\text{N II}] \lambda 6583$ and *Chandra* X-ray contour map from Iwasawa et al. (2003), and (d) $[\text{N II}] \lambda 6583/\text{H}\alpha$ ratio. North is up and east to the left. The cross in each panel marks the location of the radio continuum peak from Falcke, Wilson, & Simpson (1998). The flux scale of the emission-line maps is logarithmic, while the ratio map is on a linear scale. Refer to Iwasawa et al. (2003) for the values of the X-ray contour levels and for more detail on the X-ray data. Note the good match between the X-ray emission and the emission-line filaments above the disk of the galaxy, and the modest $[\text{N II}]/\text{H}\alpha$ ratios ($\lesssim 0.7$) in the extraplanar material.

FIG. 14.— Outer regions of NGC 4388 in (a) R0 continuum, (b) $\text{H}\alpha$, (c) $[\text{N II}] \lambda 6583$, and (d) $[\text{N II}] \lambda 6583/\text{H}\alpha$ ratio. North is up and east to the left. The cross in each panel marks the location of the radio continuum peak from Falcke, Wilson, & Simpson (1998). The flux scale of the emission-line maps is logarithmic, while the ratio map is on a linear scale. Note the modest $[\text{N II}]/\text{H}\alpha$ ratios ($\lesssim 0.7$) in the outer filaments.

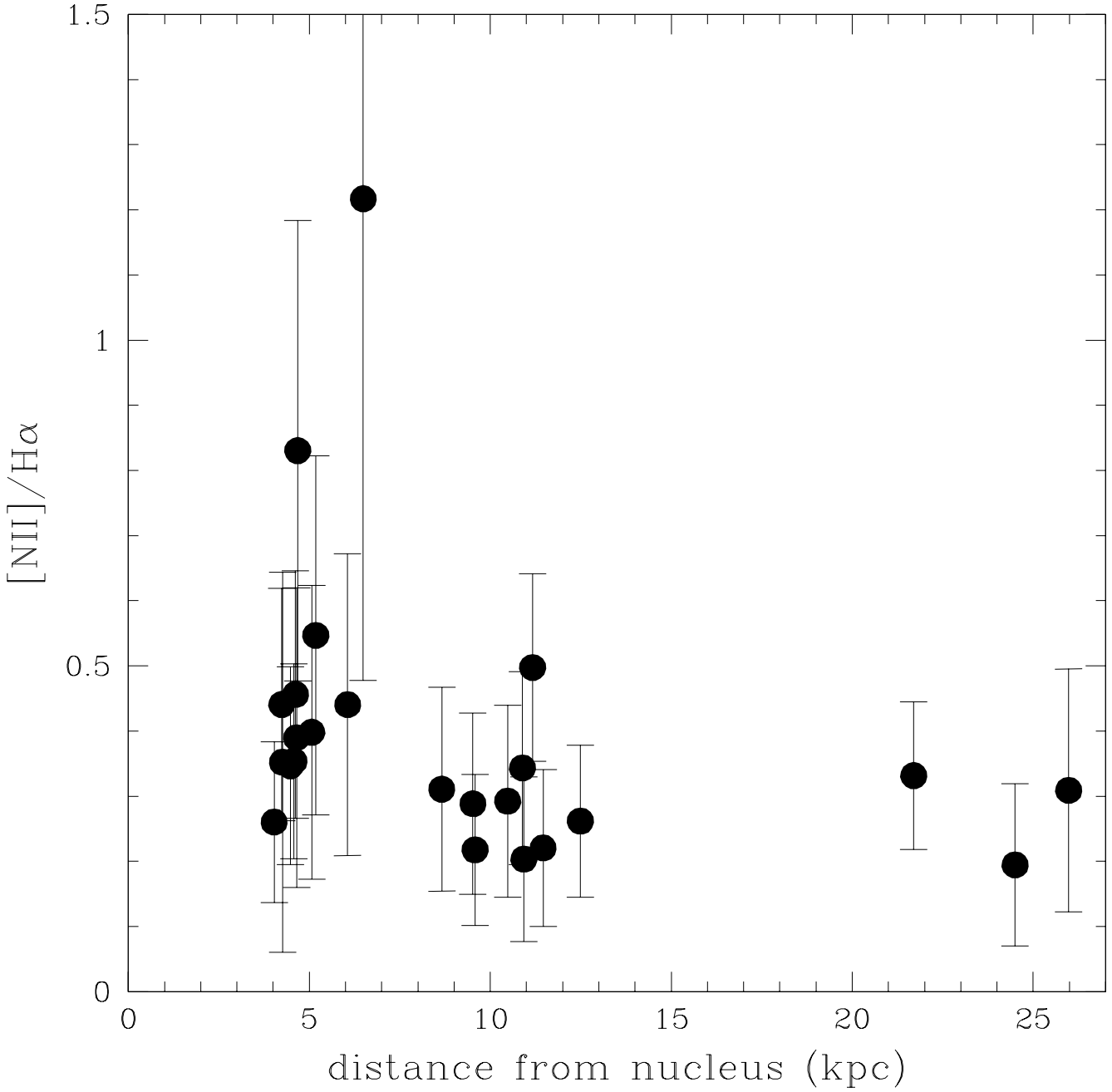


FIG. 15.— $[\text{N II}] \lambda 6583/\text{H}\alpha$ ratios as a function of galactocentric distance in NGC 4388. A 5-pixel boxcar kernel was used to smooth the $[\text{N II}]/\text{H}\alpha$ ratio map. The values shown in the figure represent the mean and $\pm 1\sigma$ around the mean calculated over regions containing from 50 to 350 pixels. The $[\text{N II}]/\text{H}\alpha$ ratios beyond ~ 7 kpc generally stay below ~ 0.7 and show no obvious gradient with distance from the nucleus.

FIG. 16.—Outer regions of NGC 6240 in (a) R0 continuum, (b) $\text{H}\alpha$, (c) $[\text{N II}] \lambda 6583$ and *Chandra* X-ray contour map from Komossa et al. (2003), and (d) $[\text{N II}] \lambda 6583/\text{H}\alpha$ ratio. North is up and east to the left. The crosses indicate the positions of the binary AGN in this object. The flux scale of the emission-line maps is logarithmic, while the ratio map is on a linear scale. The contour levels of the X-ray map are at $7.0, 14, 28$, and 111×10^{-4} counts s^{-1} arcsec^{-2} (based on an effective exposure time of 37 ksec). Complex filamentary emission extends over 70×80 kpc. Note the good match between the X-ray emission and the high- $[\text{N II}]/\text{H}\alpha$ loop and filament at $R \approx 15-25$ kpc and $\text{P.A.} \approx 270^\circ$. These features are probably associated with a galactic outflow.

FIG. 17.—Inner regions of NGC 6240 in (a) R0 continuum, (b) $\text{H}\alpha$, (c) $[\text{N II}] \lambda 6583$ and *Chandra* X-ray contour map from Komossa et al. (2003), and (d) $[\text{N II}] \lambda 6583/\text{H}\alpha$ ratio. North is up and east to the left. The crosses indicate the positions of the binary AGN in this object. The flux scale of the emission-line maps is logarithmic, while the ratio map is on a linear scale. The contour levels of the X-ray map are at $3.3, 10, 30$, and 60×10^{-4} counts s^{-1} arcsec^{-2} (based on an effective exposure time of 37 ksec). Note the good match between the brighter portions of the 5-kpc X-ray loop and a high- $[\text{N II}]/\text{H}\alpha$ feature at $R \approx 5$ kpc and $\text{P.A.} \approx 290^\circ$. Both features are probably associated with a galactic outflow.

FIG. 18.— NGC 7213 in (a) the R0 continuum, (b) $H\alpha$, (c) [N II] $\lambda 6583$, and (d) [N II] $\lambda 6583/H\alpha$ ratio. North is up and east to the left. The cross in each panel marks the location of the red continuum peak. The flux scale of the emission-line maps is logarithmic, while the ratio map is on a linear scale. A line-emitting filament is detected 19 kpc south-west of the nucleus, well beyond the optical extent of NGC 7213. The existence of this filament has been independently confirmed by Hameed et al. (2001). The broad diffuse emission off-centered from the nucleus in the TTF data is a reflective ghost.

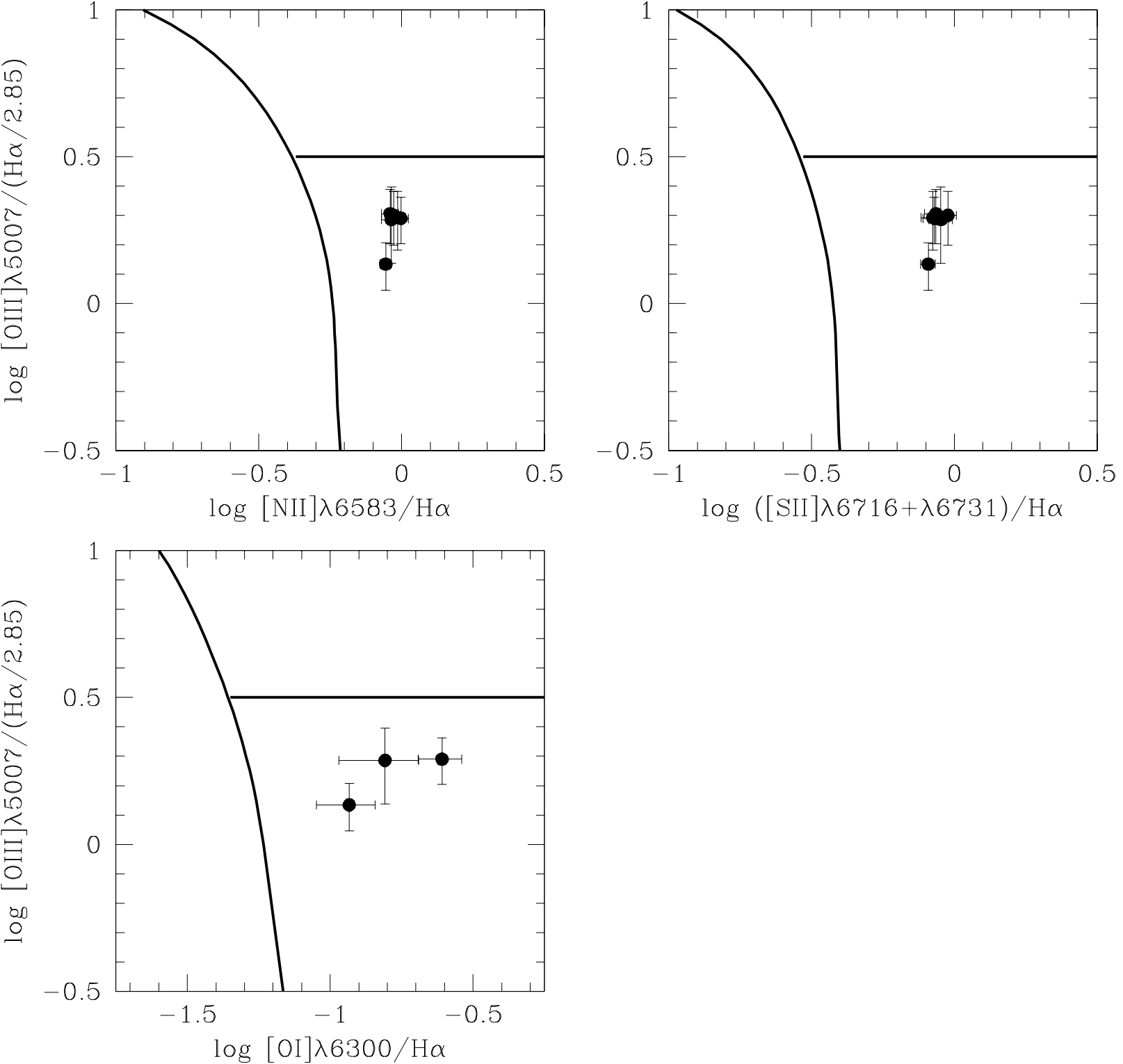


FIG. 19.— Emission-line ratios measured in the southern filament of NGC 7213. All of the line ratios are LINER-like. Given the narrow widths of the emission lines in the filament (see Fig. 20), this suggests that the filament is ionized by the diluted radiation from the central AGN rather than by shocks.

FIG. 20.— Continuum-subtracted long-slit spectrum obtained along the southern filament at $R \approx 19$ kpc and P.A. $\approx 110^\circ$. The flux scale for [O III] is linear and in units of $\text{erg s}^{-1} \text{cm}^{-2}$, while it is logarithmic for the other lines. The gas is blueshifted by $\sim 200 \text{ km s}^{-1}$ with respect to the systemic velocity, 1148 km s^{-1} . This velocity coincides with the neutral tidal gas detected by Hameed et al. (2001) at that same position.

FIG. 21.— Circinus galaxy in (a) the 2MASS K-band continuum, (b) high-resolution H α map obtained with *HST* (Wilson et al. 2000), (c) [O III] λ 5007, and (d) *Chandra* X-ray contour map from Smith & Wilson (2001) superposed on the [O III] map. North is up and east to the left. The cross in each panel marks the location of the radio/X-ray nucleus of Smith & Wilson (2001). The flux scale of the emission-line maps is logarithmic, while the ratio map is on a linear scale. Refer to Smith & Wilson (2001) for the values of the X-ray contour levels. The TTF reach a slightly fainter flux limit than the data of Veilleux & Bland-Hawthorn (1997) and reveal new emission-line features $\gtrsim 1$ kpc west and north-west from the nucleus.

FIG. 22.— ESO484-G036 in (a) the R0 continuum, (b) H α , (c) [N II] λ 6583, and (d) [N II] λ 6583/H α ratio. North is up and east to the left. The cross in each panel marks the location of the red continuum peak. The flux scale of the emission-line map is logarithmic, while the ratio map is on a linear scale. Note the cross-like structure in (c) and (d), the high-[N II]/H α extraplanar material, and the [N II]/H α minimum ~ 1 kpc south-west from the nucleus.

FIG. 23.— Deep H α and I-band images of the field surrounding the quasar MR 2251–178, reproduced from Shopbell, Veilleux, & Bland-Hawthorn (1999). Panels (a) and (b) are 1200-second exposures at redshifts of 0.0640 and 0.0645, respectively, panel (c) is an I-band continuum image of the same field, and panel (d) is a summed H α image. North is up and east to the left. The flux scale is logarithmic. A bright star (S), a nearby cluster galaxy (G1), and a number of emission-line knots from Macchetto et al. (1990) have been labeled. The emission is detected on a scale of ~ 200 kpc.

TABLE 1
SAMPLE

| Name | Redshift ^a | Nuclear Type ^b | Main Findings |
|-----------------|-----------------------|---------------------------|--|
| NGC 1068 | 0.0038 | AGN | Ionization cone detected over \sim 20-kpc scale |
| NGC 1365 | 0.0055 | AGN | Ionization cone detected over \sim 12-kpc scale |
| NGC 1482 | 0.0064 | Starburst | Galactic wind detected over \sim 20-kpc scale |
| NGC 1705 | 0.0021 | Starburst | Featureless [N II]/H α map of \sim 3-kpc wind region |
| NGC 4388 | 0.0084 | AGN | Complex of filaments detected over \sim 35-kpc scale |
| NGC 6240 | 0.0245 | AGN/Starburst | Complex of loops and filaments extending \sim 70 \times 80 kpc |
| NGC 7213 | 0.0060 | AGN | Ionized tidal filament at \sim 19 kpc from nucleus |
| Circinus Galaxy | 0.0015 | AGN/Starburst | Highly ionized filaments out to \sim 1.2 kpc from nucleus |
| ESO 484-G036 | 0.0162 | Starburst | Cross-like [N II]/H α map indicative of wind |
| MR 2251-178 | 0.0640 | QSO | Spiral-like nebula detected over \sim 200-kpc scale |

^aThe redshifts are from the NASA Extragalactic Database (NED).

^bSee text for references to the nuclear spectral type.

TABLE 2
JOURNAL OF OBSERVATIONS

| Run (1) | UT dates (2) | Telescope (3) | Instrument (4) | CCD (5) | % Dark (6) | Seeing (7) |
|------------|-----------------------|------------------|-------------------|------------|---------------|---------------------------------------|
| 1i | 1998 Aug 30, Sep 03 | AAT | RTTF | MITLL2 | 14, 47 | 1. ^{''} 3 |
| 2i | 1999 Mar 04-06 | WHT | RTTF | TEK2 | 14 | 0. ^{''} 6-1. ^{''} 8 |
| 3i | 2000 Feb 05-07, 14-16 | AAT | BTTF | MITLL3 | 22, 99 | 1. ^{''} 5 |
| 4i | 1999 Nov 28 | AAT | RTTF | MITLL2 | 43 | 1. ^{''} 0-1. ^{''} 5 |
| 5i | 2000 Feb 17-20 | AAT | BTTF | MITLL3 | 0-6 | 1. ^{''} 3-2. ^{''} 8 |
| 6i | 2000 Jul 28 | AAT | RTTF | MITLL2A | 91 | 1. ^{''} 3-1. ^{''} 6 |
| 7i | 2000 Dec 15-17 | AAT | BTTF | MITLL2A | 24-45 | 1. ^{''} 5-2. ^{''} 5 |
| 8i | 2002 May 16-20 | AAT | BTTF | EEV2 | 41-83 | 1. ^{''} 5-4. ^{''} 0 |
| 1s | 2001 Sep 18-20 | MSSSO 2.3m | DBS | SITe | 86-98 | 1. ^{''} 4-1. ^{''} 5 |
| 2s | 2001 Dec 19 | AAT | RGO 25cm | EEV2 | 79 | 1. ^{''} 7 |

Note. — Col. (1): Observing run number. Suffix “i” refers to imaging data, while suffix “s” refers to long-slit spectroscopy. (2): Dates of observations. Col. (3): Telescope used for the observations. AAT = Anglo-Australian 3.9-meter Telescope, WHT = William Herschel 4.2-meter Telescope, and MSSSO 2.3m = Mount Stromlo – Siding Springs 2.3-meter Telescope. Col.(4): Instrument used for the observations. RTTF = Red Taurus Tunable Filter, BTTF = Blue Taurus Tunable Filter, DBS = Double-Beam Spectrograph, and RGO 25cm = Royal Greenwich Observatory spectrograph equipped with 25-cm camera. Col.(5): CCD used for the observations. MITLL2/MITLL2A = 2048 \times 4096 \times 15 μ m, MITLL3 = 2048 \times 4096 \times 15 μ m (deep depletion), TEK2 = 1024 \times 1024 \times 24 μ m, EEV2 = 2048 \times 4096 \times 13 μ m (blue sensitive), and SITe = 1752 \times 532 \times 15 μ m. Col.(6): Phase of the Moon during the observations. 100% = New Moon. Col.(7): Seeing in arcseconds during the night.

TABLE 3
IMAGING OBSERVATIONS

| Object (1) | Run (2) | Line (3) | Filter/Tilt (4) | t_{exp} (5) | λ_{obs} (6) | λ_{exp} (7) | λ_{cont} (8) | $\Delta\lambda_{eff}$ (9) | CF/FS? (10) | Straddle? (11) | Sens. (12) |
|-----------------|------------|-------------------|--------------------|-----------------------------|------------------------|------------------------|-------------------------|------------------------------|----------------|-------------------|---------------|
| NGC 1068 | 2i | H α | I0/10 | 3600 | 6588 | 6588 | (I0/I1) | 11.0 | N | N | 3.0 |
| | 3i | [OIII] | B4/ 0 | 3663 | 5028 | 5026 | 4908 | 17.1 | Y | N | 15 |
| NGC 1365 | 7i | [OIII] | B4/ 0 | 2 \times 976 | 5034 | 5034 | 4994,5075 | 20.5 | Y | Y | 69 |
| | | H α | R0/15 | 1 \times 976 | 6600 | 6599 | 6554,6647 | 13.9 | Y | Y | 8.5 |
| | | [NII] | R0/15 | 1 \times 976 | 6620 | 6619 | 6555,6647 | 15.7 | Y | Y | 16 |
| NGC 1482 | 7i | H α | R0/15 | 2 \times 976 | 6606 | 6605 | 6561,6653 | 14.0 | Y | Y | 5.3 |
| | | [NII] | R0/15 | 2 \times 976 | 6627 | 6626 | 6562,6664 | 13.9 | Y | Y | 4.5 |
| | | H α | R0/15 | 3 \times 976 | 6578 | 6577 | 6533,6625 | 16.8 | Y | Y | 8.3 |
| NGC 1705 | 7i | [NII] | R0/15 | 2 \times 976 | 6597 | 6598 | 6533,6625 | 16.7 | Y | Y | 8.4 |
| | | H α | R0/15 | 4 \times 976 | 6605 | 6618 | 6551,6652 | 15.5 | Y | Y | 5.2 |
| | | [NII] | R0/15 | 6 \times 976 | 6628 | 6639 | 6554,6655 | 17.1 | Y | Y | 4.6 |
| NGC 4388 | 8i | H α | R0/15 | 6 \times 976 | 6724 | 6723 | 6670,6772 | 15.5 | Y | Y | 4.0 |
| | | [NII] | R0/ 0 | 4 \times 976 | 6743 | 6745 | 6669,6770 | 16.6 | Y | Y | 5.7 |
| | | H α | R0/ 0 | 6 \times 611 ^a | 6602,6623 | | ^a | 27.1 | Y | N | 12 |
| NGC 7213 | 4i | H α /[NII] | R0/ 0 | 6 \times 300 ^b | 6602,6623 | | ^b | 8.3 | N | N | 10 |
| | | H α /[NII] | R0/ 0 | | | | | | | | |
| | | [OIII] | B4/ 0 | 6 \times 976 | 5017 | 5014 | 4987,5048 | 19.5 | Y | Y | 39 |
| Circinus Galaxy | 5i | H α | R0/ 0 | 1 \times 976 | 6670 | 6669 | 6624,6718 | 15.9 | Y | Y | 12 |
| | | [NII] | R0/ 0 | 1 \times 976 | 6692 | 6690 | 6624,6719 | 15.9 | Y | Y | 11 |
| | | H α | R1/16 | 2 \times 600 | 6983 | 6983 | (LDSS I) | 12.4 | N | N | 2.5 |
| MR 2251–178 | 1i | H α | R1/16 | 2 \times 600 | 6986 | 6983 | (LDSS I) | 12.4 | N | N | 2.5 |
| | | H α | R1/16 | | | | | | | | |

Note. — Col. (1): Name of target. Col. (2): Run number (see Table 2). Col. (3): Emission line. [NII] = [N II] λ 6583, [OIII] = [O III] λ 5007. Col.(4): Filter used and tilt in degrees. Col.(5): Total exposure time, in seconds. Col.(6-8): Observed, expected (based on the galaxy’s systemic velocity), and continuum wavelengths at the center of each object. Col.(9): Effective bandpass in \AA . Col. (10): Use of charge shuffling and frequency switching technique (see §2). Col. (11): Use of the wavelength straddling mode (see §2). Col.(10): Sensitivity ($\sim 1-\sigma$) of observations, in units of $10^{-18} \text{ erg s}^{-1} \text{ cm}^{-2} \text{ arcsecond}^{-2}$.

^aFor run 4i, NGC 7213 was observed at 6 different wavelengths, 5 of which contain some line emission: 6585, 6594, 6603, 6625, 6634, and 6643 (all in \AA , at the location of the line-emitting filament).

^bFor run 6i, NGC 7213 was observed at 6 different wavelengths, 5 of which contain some line emission: 6594, 6615, 6617, 6620, 6626, and 6634 (all in \AA , at the location of the line-emitting filament).

TABLE 4
SPECTROSCOPIC OBSERVATIONS

| Object (1) | Run (2) | t_{exp} (3) | Slit (4) | PA (5) | description (6) |
|---------------|------------|------------------|--------------------|-----------|--------------------------------------|
| NGC 1068 | 1s | 8 \times 1800 | 2'' \times 6.7 | 6 | along filament in NE ionization cone |
| | 2s | 3 \times 1800 | 2'' \times 100'' | 3 | along filament in NE ionization cone |
| NGC 1482 | 1s | 15 \times 1200 | 2'' \times 6.7 | 103 | 15'' North - 16'' South of disk |
| | | 1 \times 600 | 2'' \times 6.7 | 103 | 5'' South of disk |
| | | 1 \times 900 | 2'' \times 6.7 | 103 | nucleus |
| | | 2 \times 300 | 2'' \times 6.7 | 103 | nucleus |
| | | 6 \times 1200 | 2'' \times 6.7 | 13 | nucleus |
| | 2s | 1 \times 1800 | 2'' \times 100'' | 13 | nucleus |
| | | 1 \times 1800 | 2'' \times 100'' | 13 | 5'' West of nucleus |
| NGC 7213 | 1s | 6 \times 1800 | 2'' \times 6.7 | 110 | along southern filament |

Note. — Col.(3): Total exposure time, in seconds. Col.(4): Slit size (width \times length), in arcseconds. Col.(5): Position angle of slit, in degrees. Col. (6): Location of the slit.

This figure "veilleux.fig1.gif" is available in "gif" format from:

<http://arxiv.org/ps/astro-ph/0308330v1>

This figure "veilleux.fig2.gif" is available in "gif" format from:

<http://arxiv.org/ps/astro-ph/0308330v1>

This figure "veilleux.fig4.gif" is available in "gif" format from:

<http://arxiv.org/ps/astro-ph/0308330v1>

This figure "veilleux.fig5.gif" is available in "gif" format from:

<http://arxiv.org/ps/astro-ph/0308330v1>

This figure "veilleux.fig6.gif" is available in "gif" format from:

<http://arxiv.org/ps/astro-ph/0308330v1>

This figure "veilleux.fig7.gif" is available in "gif" format from:

<http://arxiv.org/ps/astro-ph/0308330v1>

This figure "veilleux.fig8.gif" is available in "gif" format from:

<http://arxiv.org/ps/astro-ph/0308330v1>

This figure "veilleux.fig9.gif" is available in "gif" format from:

<http://arxiv.org/ps/astro-ph/0308330v1>

This figure "veilleux.fig10.gif" is available in "gif" format from:

<http://arxiv.org/ps/astro-ph/0308330v1>

This figure "veilleux.fig11.gif" is available in "gif" format from:

<http://arxiv.org/ps/astro-ph/0308330v1>

This figure "veilleux.fig12.gif" is available in "gif" format from:

<http://arxiv.org/ps/astro-ph/0308330v1>

This figure "veilleux.fig13.gif" is available in "gif" format from:

<http://arxiv.org/ps/astro-ph/0308330v1>

This figure "veilleux.fig14.gif" is available in "gif" format from:

<http://arxiv.org/ps/astro-ph/0308330v1>

This figure "veilleux.fig16.gif" is available in "gif" format from:

<http://arxiv.org/ps/astro-ph/0308330v1>

This figure "veilleux.fig17.gif" is available in "gif" format from:

<http://arxiv.org/ps/astro-ph/0308330v1>

This figure "veilleux.fig18.gif" is available in "gif" format from:

<http://arxiv.org/ps/astro-ph/0308330v1>

This figure "veilleux.fig20.gif" is available in "gif" format from:

<http://arxiv.org/ps/astro-ph/0308330v1>

This figure "veilleux.fig21.gif" is available in "gif" format from:

<http://arxiv.org/ps/astro-ph/0308330v1>

This figure "veilleux.fig22.gif" is available in "gif" format from:

<http://arxiv.org/ps/astro-ph/0308330v1>

This figure "veilleux.fig23.gif" is available in "gif" format from:

<http://arxiv.org/ps/astro-ph/0308330v1>